ATLAS CONF Note

ATLAS-CONF-2022-011

12th March 2022

Fiducial and differential measurements of W^+W^- production in decay topologies inspired by searches for electroweak supersymmetry in two-lepton final states

The ATLAS Collaboration

This note presents a measurement of fiducial and differential cross-sections for W^+W^- production in proton-proton collisions at $\sqrt{s}$ = 13 TeV with the ATLAS experiment at the Large Hadron Collider using a dataset corresponding to an integrated luminosity of 139 fb^{-1}. Events with exactly one electron, one muon and no hadronic jets are studied. The fiducial region in which the measurements are performed is inspired by searches for the electroweak production of supersymmetric charginos decaying to two-lepton final states and is complementary to existing ATLAS measurements. Events are selected with moderate values of missing transverse momentum and the "stransverse mass" variable m_{T2}, which is widely used in searches for supersymmetry at the LHC. The ranges of these variables are chosen to enhance direct W^+W^- production and suppress production via top quarks, which is treated as a background. Particle-level differential cross-sections for six variables are compared to theoretical predictions, with good agreement observed for all observables.

ATLAS-CONF-2022-011
29 March 2022

1 Introduction

Measurements of W^+W^- (referred to hereafter as WW) production provide important tests of the electroweak (EWK) gauge structure of the Standard Model (SM) of particle physics, and WW production also represents an important background process in searches for Beyond-the-SM (BSM) physics. In searches for supersymmetry [1–6] (SUSY) where WW represents a significant background, a semi-data-driven approach is often taken which involves normalising the simulated Monte Carlo (MC) samples to data in a control region (CR), designed to be kinematically similar to the search regions but enriched in SM WW production. Significant differences from unity of these scaling factors suggest mismodelling in the phase space targeted by the search, but can be difficult to compare to results of precision SM measurements as they refer to detector-level quantities. Producing "unfolded" particle-level measurements in event topologies associated with search results represents a novel way to address this. The ATLAS experiment [7] has previously released differential measurements of $t\bar{t}$ and Z+jets production regions related to the control regions of a search for leptoquarks in dilepton+dijet events [8]. This note presents the first effort to produce measurements in topologies associated with SUSY searches that are complementary to existing ATLAS measurements.

Inclusive and fiducial WW production cross-sections have been measured in proton–proton (pp) collisions at $\sqrt{s} = 7$ TeV [9, 10], 8 TeV [11–13] and 13 TeV [14–17], as well as in e^+e^- collisions at LEP [18] and in $p\bar{p}$ collisions at the Tevatron [19–21]. This analysis complements existing ATLAS 13 TeV measurements of WW production in 0-jet events [15] and in $\geq$ 1-jet events [16] by measuring differential cross-sections in a fiducial region close to the WW control region from a previous search for the electroweak production of supersymmetric charginos or sleptons [22]. This search targeted the electroweak production of SUSY particles decaying to final states with 2 leptons (electrons or muons) and missing transverse momentum using 139 fb^{-1} of pp-collisions at 13 TeV collected during Run-2 of the LHC and is referred to hereafter as the "EWK 2ℓ+0-jets search". WW production was the main background process in this search and the associated theoretical uncertainties were among the dominant systematic uncertainties in the search regions. By targeting more extreme event topologies compared to conventional SM measurements this result can be used to provide additional constraints on BSM physics, and improve the modelling of the SM backgrounds for future searches.

The $WW \to e^{\pm}\nu\mu^{\mp}\nu$ decay channel is studied in events with no identified jets with a transverse momentum $p_{\mathrm{T}} > 20$ GeV and pseudorapidity $|\eta| < 2.4$[1], and with values of the magnitude of the missing transverse momentum, $E_{\mathrm{T}}^{\mathrm{miss}}$, between 60 and 80 GeV. Missing transverse momentum is calculated to represent the momentum imbalance in the plane transverse to the colliding beams. High values of $E_{\mathrm{T}}^{\mathrm{miss}}$ can be generated by weakly interacting neutral particles escaping the detector, which is thus an important variable in many BSM searches. This analysis also considers more stringent requirements on the dilepton invariant mass compared to the 36 fb^{-1} WW+0-jet measurement [15]. The dominant background process is top quark production ($t\bar{t}$ and single-top Wt), which is estimated using the same data-driven method as was used in the EWK 2ℓ+0-jets search. The measurements are performed in a fiducial phase space close to the geometric and kinematic acceptance of the experimental analysis. Differential cross-section measurements are performed for six variables, which are the same as those considered in the 36 fb^{-1} WW+0-jet measurement [15]:

[1] ATLAS uses a right-handed coordinate system with its origin at the nominal interaction point (IP) in the centre of the detector and the z-axis along the beam pipe. The x-axis points from the IP to the centre of the LHC ring, and the y-axis points upward. Cylindrical coordinates (r, ϕ) are used in the transverse plane, ϕ being the azimuthal angle around the z-axis. The pseudorapidity is defined in terms of the polar angle θ as $\eta = -\ln\tan(\theta/2)$

- The azimuthal separation between the two leptons $|\Delta\phi_{e\mu}|$.
- The rapidity of the dilepton system $|y_{e\mu}|$.
- $\cos\theta^* = |\tanh(\Delta y(e\mu)/2)|$, which is longitudinally boost invariant and sensitive to the spin structure of the produced diparticle pairs [23], and where $\Delta y(e\mu)$ is the difference in rapidity between the electron and the muon.
- The transverse momentum of the leading lepton $p_{\mathrm{T}}^{\mathrm{lead}\,\ell}$.
- The invariant mass of the dilepton system $m_{e\mu}$.
- The transverse momentum of the dilepton system $p_{\mathrm{T}}^{e\mu}$.

In this note $|\Delta\phi_{e\mu}|$, $|y_{e\mu}|$ and $\cos\theta^*$ are referred to collectively as "angular" variables, as they probe angular correlations and are sensitive to the spin structure of the WW production system, and $p_{\mathrm{T}}^{\mathrm{lead}\,\ell}$, $m_{e\mu}$ and $p_{\mathrm{T}}^{e\mu}$ are referred to collectively as "scale" variables, as they characterise the energy of the process.

This note is structured as follows: Section 2 describes the ATLAS detector, then Section 3 presents the analysis that is performed to produce the fiducial and differential cross-section measurements. This includes the data and MC samples used, the reconstructed object definitions and event selections used to define the detector-level signal regions, the SM background estimation, as well as the systematic uncertainties considered and the unfolding techniques used to correct detector-level information back to particle level. Finally, the results are reported in Section 4 and Section 5 summarises the conclusions.

2 ATLAS detector

The ATLAS experiment at the LHC is a multipurpose particle detector with a forward–backward symmetric cylindrical geometry and a near 4π coverage in solid angle. It consists of an inner tracking detector surrounded by a thin superconducting solenoid providing a 2 T axial magnetic field, electromagnetic and hadron calorimeters, and a muon spectrometer. The inner tracking detector covers the pseudorapidity range $|\eta| < 2.5$. It consists of silicon pixel, silicon microstrip, and transition radiation tracking detectors. Lead/liquid-argon (LAr) sampling calorimeters provide electromagnetic (EM) energy measurements with high granularity. A steel/scintillator-tile hadron calorimeter covers the central pseudorapidity range ($|\eta| < 1.7$). The endcap and forward regions are instrumented with LAr calorimeters for both the EM and hadronic energy measurements up to $|\eta| = 4.9$. The muon spectrometer surrounds the calorimeters and is based on three large superconducting air-core toroidal magnets with eight coils each. The field integral of the toroids ranges between 2.0 and 6.0 T m across most of the detector. The muon spectrometer includes a system of precision tracking chambers and fast detectors for triggering. A two-level trigger system is used to select events. The first-level trigger is implemented in hardware and uses a subset of the detector information to accept events at a rate below 100 kHz. This is followed by a software-based trigger that reduces the accepted event rate to 1 kHz on average depending on the data-taking conditions. An extensive software suite [24] is used in the reconstruction and analysis of real and simulated data, in detector operations, and in the trigger and data acquisition systems of the experiment.

3 Analysis

3.1 Data and simulated event samples

This analysis uses pp collision data at a centre-of-mass energy of $\sqrt{s}$ = 13 TeV collected by the ATLAS detector during the second data-taking run of the LHC, which took place between 2015 and 2018. After requiring standard data-quality requirements on LHC and detector operations [25], this dataset corresponds to a total integrated luminosity of 139 fb^{-1} with an uncertainty of 1.7% [26], obtained using the LUCID-2 detector [27] for the primary luminosity measurements. Candidate events were selected by a trigger that required at least one electron-muon pair [28, 29]. The trigger-level thresholds for the transverse momentum, p_{T}, of the leptons involved in the trigger decision were 17 GeV for the electron and 14 GeV for the muon. The thresholds applied in the lepton offline selection ensured that trigger efficiencies are constant in the relevant phase space.

Simulated MC samples are used for the SM background estimates and to correct the signal distributions for detector effects. These were processed through a full simulation of the ATLAS detector [30] based on GEANT4 [31] and reconstructed with the same algorithms as those used for the data. The generation of the simulated event samples includes the effect of multiple pp interactions per bunch crossing (pile-up), as well as the effect on the detector response due to interactions from bunch crossings before or after the one containing the hard interaction. Differences between data and simulation in the lepton reconstruction efficiency, energy scale, energy resolution and modelling of the trigger [32, 33], and in the b-tagging efficiency [34] are treated through correction factors that are derived from data and applied as weights to the simulated events. The MC samples are also reweighted so that the distribution of the average number of interactions per bunch crossing reproduces the observed distribution in the data.

WW signal samples are generated by summing $q\bar{q}$ and gg-initiated samples. The $q\bar{q}$-initiated WW signal is simulated at next-to leading order (NLO) accuracy in QCD using the POWHEG BOX v2 [35–37] generator interfaced to PYTHIA 8.186 [38] for the modelling of the parton shower, hadronisation, and underlying events, with parameters set according to the AZNLO tune [39]. The CT10 NLO PDF set [40] was used for the hard-scattering processes, whereas the CTEQ6L1 PDF set [41] was used for the parton shower [42]. The events were normalised to the next-to-next-to leading order (NNLO) in QCD cross-section [43]. Loop-induced $gg \to WW \to \ell\nu\ell\nu$ are simulated at LO with up to one additional parton emission using SHERPA v2.2.2, with virtual QCD corrections provided by the OPENLOOPS library [42, 44–46]. The $gg \to WW$ process was normalised to its inclusive NLO QCD cross-section [47]. This is labelled as "Sherpa+OL" in all plots and tables in the results of this note. An alternative sample of events for $q\bar{q} \to WW$ is simulated using the SHERPA v2.2.2 [42, 48] with matrix elements at NLO accuracy in QCD for up to one additional parton and at LO accuracy for up to three additional parton emissions. For the SHERPA $q\bar{q}$- and gg- initiated samples the NNPDF3.0NNLO set of PDFs was used [49], along with the dedicated set of tuned parton-shower parameters developed by the SHERPA authors. No alternative simulation is considered for the $gg \to WW$ initial state which makes up a small fraction of the signal.

Table 1 summarises the generators used for the SM backgrounds along with the relevant parton distribution function (PDF) sets, the tuned set of parameters for the configuration of underlying-event and hadronisation, and the cross-section order in α_{s} used to normalise the event yields for these samples. This study uses the same simulated samples and groupings for the SM background processes as the EWK 2ℓ+0-jets search [22]. The "other" category groups together processes that represented small or negligible contributions to the "signal regions" of the search, which include Drell–Yan, $t\bar{t}$ +V and Higgs boson production. Further

information on the simulations of $t\bar{t}$, single top (Wt), multiboson and boson plus jet processes can also be found in the relevant public ATLAS notes [42, 50–52].

Table 1: Simulated background event samples with the corresponding matrix element and parton shower (PS) generators, cross-section order in α_s used to normalise the event yield, underlying-event tune and the generator PDF sets used. Where used the label "V" refers to W or Z.

Label	Physics process	Generator	Parton shower	Normalisation in QCD	Tune	PDF (generator)	PDF (PS)
$t\bar{t}$	$t\bar{t}$	Powheg Box v2 [36, 53–55]	Pythia 8.230 [56]	NNLO+NNLL [57]	A14 [58]	NNPDF3.0NLO [49]	NNPDF2.3LO [59]
Single top	Single top (Wt)	Powheg Box v2 [36, 54, 60]	Pythia 8.230	NLO+NNLL [61, 62]	A14	NNPDF3.0NLO	NNPDF2.3LO
VZ	WZ, ZZ	Powheg Box v2 [36, 54, 63, 64]	Pythia 8.210	NLO [42, 63, 64]	AZNLO [39]	CT10 NLO [40]	CTEQ6L1[65]
"Others"	Higgs	Powheg Box v2 [35–37]	Pythia 8.212 [56]	NNNLO+NNLL [66–72]	AZNLO [39]	PDF4LHC15nnlo [73]	CTEQ6L1
	VVV	Sherpa 2.2.2 [42, 48, 74]	Sherpa 2.2.2	NLO [42, 48]	Sherpa default [42]	NNPDF3.0NNLO	NNPDF3.0NNLO
	$t\bar{t}+H$	MadGraph5_aMC@NLO [75]	Pythia 8.230 [56]	NLO [66]	A14	NNPDF3.0NLO	NNPDF2.3LO
	$t\bar{t}+V$	MadGraph5_aMC@NLO	Pythia 8.210 [56]	NLO [75, 76]	A14	NNPDF3.0NLO	NNPDF2.3LO
	$t\bar{t}+WW$	MadGraph5_aMC@NLO	Pythia 8.186 [38]	NLO [75]	A14	NNPDF2.3LO	NNPDF2.3LO
	$tZ, t\bar{t}t\bar{t}, t\bar{t}t$	MadGraph5_aMC@NLO	Pythia 8.230	NLO [75]	A14	NNPDF3.0NLO	NNPDF2.3LO
	$Z/\gamma(\rightarrow ll)$+jets	Sherpa2.2.1 [48, 74, 77]	Sherpa 2.2.1	NNLO [78]	Sherpa default [77]	NNPDF3.0NNLO [49]	NNPDF3.0NNLO [49]

3.2 Event reconstruction and selection

Events are required to have at least one reconstructed vertex with at least two associated tracks with $p_{\mathrm{T}} > 400$ MeV. When more than one vertices are reconstructed, the one with the highest $\sum p_{\mathrm{T}}^2$ of associated tracks is taken to be the primary vertex. All final-state objects (electrons, muons and jets in this study) are required to satisfy "baseline" criteria to ensure they are well-reconstructed and originate from the primary vertex, and additional "signal" criteria are applied to define the objects used in the measurement. Baseline electrons (muons) are required to have $p_{\mathrm{T}} > 10$ GeV, pseudorapidity $|\eta| < 2.47$ (2.6) and be within $|z_0 \sin\theta| = 0.5$ mm of the primary vertex. Electrons are required to satisfy a *Loose* likelihood-based identification requirement [32], while muons are required to satisfy the *Medium* identification requirements defined in Ref. [33]. Signal electrons are required to satisfy a *Tight* identification requirement [32] and the track associated with the signal electron is required to have $|d_0|/\sigma(d_0) < 5$, where d_0 is the transverse impact parameter relative to the reconstructed primary vertex and $\sigma(d_0)$ is its uncertainty, whilst for signal muons the associated track must have $|d_0|/\sigma(d_0) < 3$. The signal lepton isolation criteria used in the EWK 2ℓ+0-jets search [22] are also applied in this study. Hadronic jets are reconstructed from topological clusters formed from energy deposits in calorimetric cells [79, 80] using the anti-k_t jet clustering algorithm [81] as implemented in the FastJet package [82], with a radius parameter $R = 0.4$. They are then calibrated by the application of a jet energy scale derived from 13 TeV data and simulation [83]. To reduce the effects of pile-up, for jets with $|\eta| < 2.5$ and $p_{\mathrm{T}} < 120$ GeV a significant fraction of the tracks associated with each jet are required to have an origin compatible with the primary vertex, as defined by the jet vertex tagger [84]. For jets with $|\eta| > 2.5$ and $p_{\mathrm{T}} < 60$ GeV, similar pile-up suppression is achieved through the forward jet vertex tagger [85]. Finally, events are rejected if they contain a jet that does not satisfy the jet-quality requirements [86, 87] in order to remove events impacted by detector noise and non-collision backgrounds. Jets containing b-hadrons ("b-jets") are identified using the MV2c10 boosted decision tree algorithm [34] which uses quantities such as the impact parameters of associated tracks, and well-reconstructed secondary vertices. A selection that provides 85% efficiency for tagging b-jets in simulated $t\bar{t}$ events is used in this study. Only jet candidates with $p_{\mathrm{T}} > 20$ GeV and $|\eta| < 2.4$ are considered[2], although jets with $|\eta| < 4.9$

[2] Hadronic τ-lepton decay products are treated as jets.

are included in the missing transverse momentum calculation and the procedure to remove reconstruction ambiguities that could lead to double counting of baseline objects. This is applied as follows:

- jet candidates within $\Delta R' = \sqrt{(\Delta y)^2 + (\Delta\phi)^2} = 0.2$ of an electron candidate are removed;
- jets with fewer than three tracks that lie within $\Delta R' = 0.4$ of a muon candidate are removed;
- electrons and muons within $\Delta R' = 0.4$ of the remaining jets are discarded, to reject leptons from the decay of b- or c-hadrons;
- electron candidates are rejected if they are found to share an inner detector track with a muon.

The measurements are performed in events with exactly one signal electron and one signal muon with opposite electric charge and each satisfying $p_{\mathrm{T}} > 20$ GeV, and a veto on additional baseline leptons with and hadronic jets . The multiplicity of non-b-tagged and b-tagged jets are considered separately in the background estimation of this study: events with exactly one b-tagged jet with a veto on additional non-b-tagged jets are used to estimate and validate the top-quark background. Requirements are also placed on the missing transverse momentum ($\mathbf{p}_{\mathrm{T}}^{\mathrm{miss}}$), which has magnitude $E_{\mathrm{T}}^{\mathrm{miss}}$. This is defined as the negative vector sum of the transverse momenta of all identified physics objects (electrons, photons, muons and jets). Low-momentum tracks from the primary vertex that are not associated with reconstructed analysis objects are also included in the calculation through the soft term of $E_{\mathrm{T}}^{\mathrm{miss}}$. The $E_{\mathrm{T}}^{\mathrm{miss}}$ value is adjusted for the calibration of the selected physics objects [88].

The additional requirements used to access the regions of phase space probed in the EWK 2ℓ+0-jets search are as follows:

- The invariant mass of the dilepton system $m_{e\mu} > 100$ GeV .
- The magnitude of the missing transverse momentum vector, $E_{\mathrm{T}}^{\mathrm{miss}} \in$ [60,80] GeV.
- The "stransverse mass" variable, $m_{\mathrm{T2}} \in$ [60,80] GeV [89, 90]. m_{T2} is defined in Equation (1),

$$m_{\mathrm{T2}}(\mathbf{p}_{\mathrm{T},1}, \mathbf{p}_{\mathrm{T},2}, \mathbf{p}_{\mathrm{T}}^{\mathrm{miss}}) = \min_{\mathbf{q}_{\mathrm{T},1}+\mathbf{q}_{\mathrm{T},2}=\mathbf{p}_{\mathrm{T}}^{\mathrm{miss}}} \left\{ \max[\, m_{\mathrm{T}}(\mathbf{p}_{\mathrm{T},1}, \mathbf{q}_{\mathrm{T},1}), m_{\mathrm{T}}(\mathbf{p}_{\mathrm{T},2}, \mathbf{q}_{\mathrm{T},2}) \,] \right\}, \tag{1}$$

  where m_{T} indicates the transverse mass which is defined as $m_{\mathrm{T}} = \sqrt{2 \times |\mathbf{p}_{\mathrm{T,a}}| \times |\mathbf{p}_{\mathrm{T,b}}| \times (1 - \cos(\Delta\phi))}$, and $\Delta\phi$ is the difference in azimuthal angle between the particles with transverse momenta $\mathbf{p}_{\mathrm{T,a}}$ and $\mathbf{p}_{\mathrm{T,b}}$. $\mathbf{p}_{\mathrm{T},1}$ and $\mathbf{p}_{\mathrm{T},2}$ are the transverse-momentum vectors of the two leptons, and $\mathbf{q}_{\mathrm{T},1}$ and $\mathbf{q}_{\mathrm{T},2}$ are vectors with $\mathbf{p}_{\mathrm{T}}^{\mathrm{miss}} = \mathbf{q}_{\mathrm{T},1} + \mathbf{q}_{\mathrm{T},2}$. This variable was designed to be sensitive to the mass scales of pair-produced heavy particles that each decay semi-invisibly. The minimisation is performed over all the possible decompositions of $\mathbf{p}_{\mathrm{T}}^{\mathrm{miss}}$ into two hypothetical invisible particles with momenta $\mathbf{q}_{\mathrm{T},1}$ and $\mathbf{q}_{\mathrm{T},2}$. For $t\bar{t}$ or WW decays, assuming an ideal detector with perfect momentum resolution, $m_{\mathrm{T2}}(\mathbf{p}_{\mathrm{T},\ell_1}, \mathbf{p}_{\mathrm{T},\ell_2}, \mathbf{p}_{\mathrm{T}}^{\mathrm{miss}})$ has a kinematic endpoint at the mass of the W boson [90]. The signal regions of the EWK 2ℓ+0-jets required high values of $m_{\mathrm{T2}} >$ 100 GeV.

For the EWK 2ℓ+0-jets search the top contamination in events with a jet veto was observed to increase with m_{T2} in the region $m_{\mathrm{T2}} \in$ [60,100] GeV. To maximise WW purity, the control region required $m_{\mathrm{T2}} \in$ [60,65] GeV and $E_{\mathrm{T}}^{\mathrm{miss}} \in$ [60,100] GeV with validation of the estimate being performed in events with $m_{\mathrm{T2}} \in$ [65,100] GeV and $E_{\mathrm{T}}^{\mathrm{miss}} > 60$ GeV. As m_{T2} is sensitive to the angular separation of the lepton pair, the m_{T2} range is widened for the analysis described in this note to provide a broader phase space for measuring angular distributions. As $E_{\mathrm{T}}^{\mathrm{miss}}$ and m_{T2} are correlated, the $E_{\mathrm{T}}^{\mathrm{miss}}$ range is tightened to reduce the top contamination. These changes result in a higher statistics region to perform the differential measurements

without reducing the WW purity. The requirement on the "object-based $E_{\mathrm{T}}^{\mathrm{miss}}$ significance" [91] is also removed, to simplify the definition of the fiducial region at particle level[3]. The definition of the signal region considered in this study is summarised in Table 2. The same selections are used at particle level when defining the fiducial region used for the fiducial and differential cross-section calculation, as discussed in Section 3.4.

Table 2: Summary of the selection criteria used for the signal region. The same selections are used at detector and at particle level.

Selection requirement	Criteria
Lepton flavour	$e^{\pm}\mu^{\mp}$
Lepton p_{T}	> 25 GeV
Lepton $\lvert\eta\rvert$	$< 2.47 (e^{\pm}), < 2.6 (\mu^{\mp})$
Lepton veto	No additional electrons with $p_{\mathrm{T}} > 10$ GeV, $\lvert\eta\rvert < 2.47$
	No additional muons with $p_{\mathrm{T}} > 10$ GeV, $\lvert\eta\rvert < 2.6$
$m_{e\mu}$	> 100 GeV
Jet veto	No jets with $p_{\mathrm{T}} > 20$ GeV, $\lvert\eta\rvert < 2.4$
m_{T2}	$\in$ [60,80] GeV
$E_{\mathrm{T}}^{\mathrm{miss}}$	$\in$ [60,80] GeV

Figure 1 shows detector-level comparisons of data and the SM processes for the six variables that will be unfolded to particle level in this study.

[3] The 'object-based $E_{\mathrm{T}}^{\mathrm{miss}}$ significance' helps to separate events with true $E_{\mathrm{T}}^{\mathrm{miss}}$ (arising from weakly interacting particles) from those where it is consistent with particle mismeasurement, resolution or identification inefficiencies. On an event-by-event basis, given the full event composition, $E_{\mathrm{T}}^{\mathrm{miss}}$ significance evaluates the p-value that the observed $E_{\mathrm{T}}^{\mathrm{miss}}$ is consistent with the null hypothesis of zero real $E_{\mathrm{T}}^{\mathrm{miss}}$, as further detailed in Ref. [91].

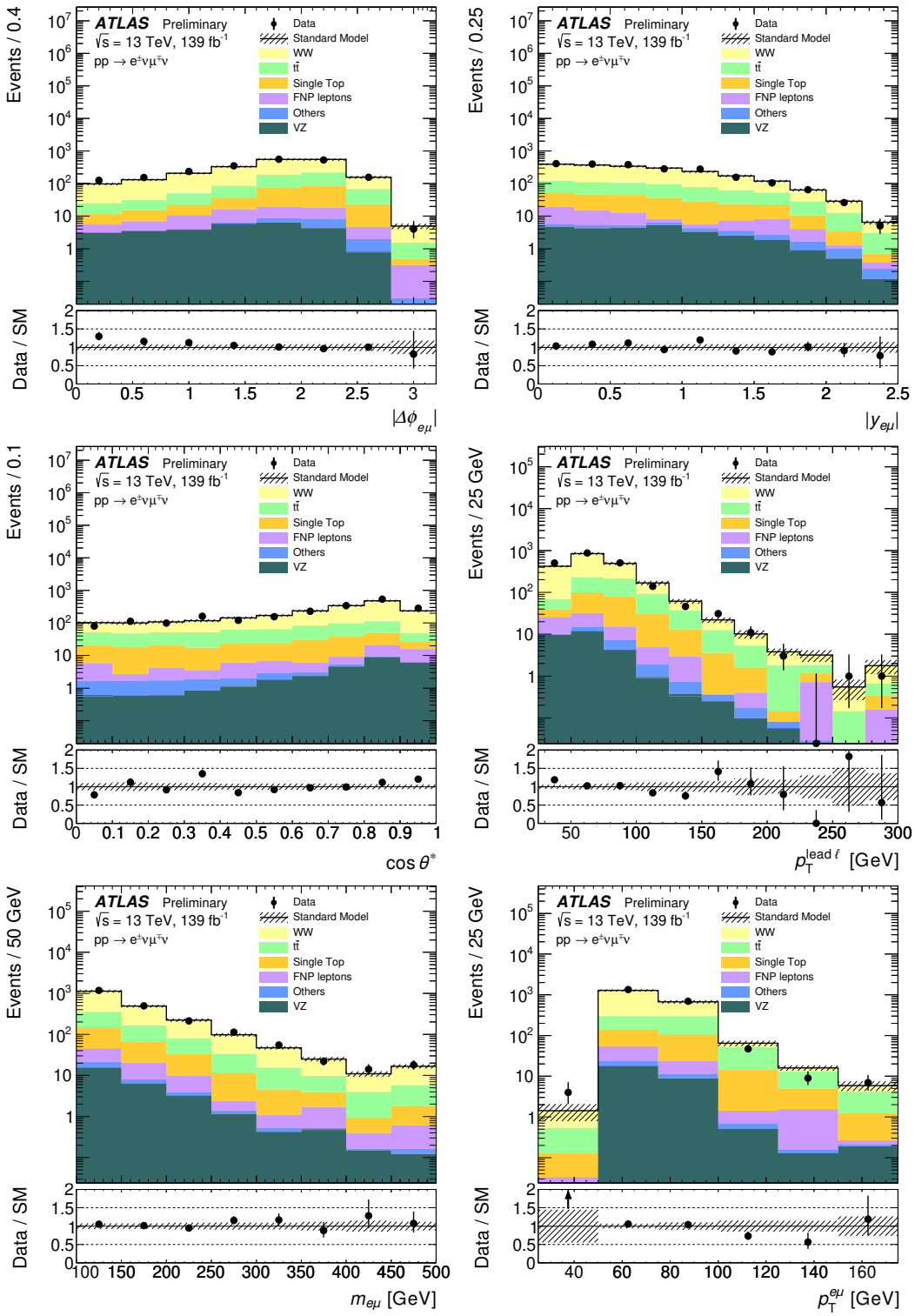

Figure 1: Signal-region detector level distributions of $|\Delta\phi_{e\mu}|$ (top left), $|y_{e\mu}|$ (top right), $\cos\theta^*$ (middle left), $p_{\mathrm{T}}^{\mathrm{lead}\,\ell}$ (middle right), $m_{e\mu}$ (bottom left), $p_{\mathrm{T}}^{e\mu}$ (bottom right). Data is indicated by black markers along with the distribution for the WW signal and background SM processes. The last bins of the scale variable distributions contain overflow events. The lower panels show the ratio of data to the total SM background prediction. The uncertainty bands shown include statistical and systematic uncertainties, excluding theory uncertainties on the WW signal. "FNP" refers to the fake-non-prompt lepton background and is calculated using the data-driven matrix method.

3.3 Background estimation

The estimation of the SM backgrounds in this study uses the same techniques as those used in the EWK 2ℓ+0-jets search [22]. For the search the SM backgrounds were classified into irreducible backgrounds from processes producing prompt leptons and reducible processes containing one or more fake/non-prompt (FNP) leptons. The main irreducible backgrounds were SM diboson (WW, WZ, ZZ) and top-quark ($t\bar{t}$ and Wt) production which were estimated from simulated events, normalised using a simultaneous likelihood fit to data in dedicated control regions (CRs). The yields and shapes of kinematic distributions of the relevant backgrounds were then validated in a set of validation regions (VRs). Three CRs were used: CR-WW, targeting WW production; CR-VZ, targeting WZ and ZZ production, which are normalised by using a single parameter in the likelihood fit to the data; and CR-top, targeting $t\bar{t}$ and single-top-quark production, which are also normalised by using a single parameter in the likelihood fit to the data. Both CR-VZ and CR-top require high m_{T2}, and high values of missing transverse momentum and its significance. CR-VZ uses same-flavour (dielectron and dimuon) events with a jet veto and requires the dilepton invariant mass to be consistent with an on-shell Z boson. CR-top requires one electron and one muon, one b-tagged jets with a veto on additional non-b-tagged jets. The remaining background from FNP leptons is estimated from data using the matrix method (MM) [92]. In this study, WW is the target signal process, with the remaining processes being backgrounds that are subtracted from the data prior to calculating the fiducial and differential cross-sections.

The statistical interpretation for the search was performed using the HistFitter framework [93]. The likelihood for the "background-only" fit used to constrain the background normalisation factors was a product of Poisson probability density functions describing the observed number of events in each CR and Gaussian distributions that constrain the nuisance parameters associated with the systematic uncertainties. Poisson distributions are used for MC statistical uncertainties. Further details of the likelihood fit can be found in the EWK 2ℓ+0-jets search paper [22]. After the fit, the normalisation factors returned for the WW, $t\bar{t}$ and single-top-quark, and WZ/ZZ processes were 1.25 ± 0.11, 0.82 ± 0.06 and 1.18 ± 0.05 respectively, which for diboson processes were applied to MC samples scaled to NLO QCD cross-sections (the NNLO QCD cross-sections were not applied in the original search paper as the samples were normalised to the data in the control regions). Good agreement, within about one standard deviation, was observed for the yields and kinematic distributions in all VRs when applying these normalisation factors and their corresponding uncertainties. The deviation from unity of the WW normalisation factor by more than 1σ suggests a tension between the SM and data in the parameter space probed by the search that will be tested further in this study.

In this study, the normalisation factors from the EWK 2ℓ+0-jets search are directly applied to the VZ (WZ/ZZ) and top ($t\bar{t}$,Wt) backgrounds that are subtracted from the data when performing the cross-section measurements described in Section 3.4. The uncertainties on the normalisation factors are propagated through the calculation as discussed in Section 3.5. The correlations and constraints introduced by the likelihood fit on the nuisance parameters describing the systematic uncertainties are not applied in this study, which are instead assumed to take their nominal values as discussed in Section 3.5. This approach is designed to be conservative, however as no significant constraints were observed in the EWK 2ℓ+0-jets search this choice has a negligible impact on the results. To validate the use of the original top normalisation factor from the EWK 2ℓ+0-jets search in the adjusted phase space of this study, an additional validation exercise is performed to check the modelling of the top quark background in a region with the same selection as Table 2 but requiring exactly one b-tagged jet. Good agreement is observed across all six distributions considered for differential cross-section measurements.

3.4 Fiducial cross-section determination

The differential cross-sections are measured in the fiducial phase space of the $WW \to e^{\pm}\nu\mu^{\mp}\nu$ decay channel using particle-level implementations of the selection criteria defined in Table 2. Electrons and muons are required to originate from the hard interaction and not from hadron decays. Electrons and muons from leptonically decaying τ leptons are included in the fiducial region. The momenta of photons emitted in a cone of size $\Delta R = 0.1$ around the lepton direction that do not originate from hadron decays are added to form "dressed" leptons. Particle-level jets are reconstructed using the anti-k_t algorithm [81] with radius parameter $R = 0.4$ from stable final-state particles, excluding prompt dressed leptons. The particle-level missing transverse momentum is defined as the vectorial sum of the momenta of invisible particles in the event. For SM processes this is the sum of the neutrino momenta.

The fiducial cross-section is calculated as:

$$\sigma_{WW} = \frac{N_{\text{obs}} - N_{\text{bkg}}}{C \cdot \mathcal{L}},$$

where N_{obs} is the observed number of data-events in the fiducial region, N_{bkg} is the predicted number of background events, $\mathcal{L}$ the integrated luminosity, and C is a correction factor of the observation due to limited acceptances and detector inefficiencies. It is calculated using MC as the number of simulated signal events passing the detector level event selection divided by the number of events in the fiducial phase space. In this study $C = 0.55 \pm 0.08$ has been applied, where the uncertainties include statistical, experimental and theoretical sources, as described in Section 3.5.

The differential cross-sections are calculated using the Iterative Bayesian Unfolding (IBU) technique [94, 95] as implemented in the RooUnfold package [96]. This unfolding technique corrects the detector-level distributions of data (with the non-WW backgrounds subtracted) for migrations between bins introduced by the event reconstruction. It also applies fiducial corrections (corresponding to events that are reconstructed in the signal region but originate outside the fiducial region at particle level) and reconstruction efficiency corrections (due to events that lie inside the fiducial region at particle level but do not enter the signal region due to detector inefficiencies). The bins chosen for the differential measurements were optimised to avoid too high statistical uncertainties in the measurements and to reduce the migration of events between particle-level and detector-level bins. The number of iterations used in IBU is also optimised by considering the resulting statistical uncertainty on the measurement and the bias due to the assumed true distribution, with too many iterations generating high statistical uncertainties and too few iterations causing bias in the measurements towards the MC prediction. In this study, two iterations are chosen for $\cos\theta^*$ and $|\Delta\phi_{e\mu}|$, three iterations are used for $m_{e\mu}$ and $p_{\text{T}}^{\text{lead}\,\ell}$, and four iterations are used for $|y_{e\mu}|$ and $p_{\text{T}}^{e\mu}$. In addition to the bias tests discussed in Section 3.5 to measure any systematic effects due to the use of the signal WW MC sample in the unfolding procedure, several signal injection tests were performed using SUSY models for chargino-pair production that were on the edge of the exclusion sensitivity in the EWK 2ℓ+0-jets search. These are important checks for the validity of using these measurements to calculate constraints on BSM physics. Detector level distributions of WW plus injected BSM signal were input to the unfolding calculation to test if the particle-level WW plus BSM distribution could be recovered. The unfolding calculation matched the expected WW plus BSM distributions for a range of SUSY models displaying different kinematics due to their SUSY masses.

3.5 Systematic uncertainties

Systematic uncertainties in the WW differential cross-section measurements calculated in this study arise from experimental sources (which impact the subtracted non-WW backgrounds, and the calculation used to correct the signal for detector effects), uncertainties in the modelling of the top background (which includes theoretical uncertainties, and uncertainties associated with the data-driven background estimate), and signal modelling. Statistical uncertainties associated with the MC samples used for the signal and background processes, and the observed data distributions also impact the unfolded distributions.

The same sources of experimental uncertainties as those considered in the EWK 2ℓ+0-jets search [22] are used in this study. The dominant experimental uncertainties are due to the calibration of the jet energy scale and resolution [80, 83]. Additional uncertainties that arise from lepton reconstruction efficiency, lepton energy scale and lepton energy resolution and differences between the trigger efficiencies in data and simulation are grouped into the lepton uncertainties category. There are also uncertainties in the scale factors applied to the simulated samples to account for differences between data and simulation in the b-jet identification efficiency, and an uncertainty in $\mathbf{p}_{\mathrm{T}}^{\mathrm{miss}}$ associated with the soft-term resolution and scale [88]. Finally, an uncertainty is applied for the reweighting procedure (pile-up reweighting) applied to simulated events to match the distribution of the number of interactions per bunch crossing observed in data.

For the subtracted-backgrounds, several sources of uncertainty on the modelling of $t\bar{t}$ and Wt are considered by varying the normalisation and shape of the subtracted backgrounds. For $t\bar{t}$ production, uncertainties in the parton shower simulation are estimated by comparing samples generated with Powheg Box interfaced to either Pythia v8.186 or Herwig 7.04 [97, 98]. Uncertainties in the modelling of initial- and final-state radiation are calculated by comparing the predictions of the nominal sample with two alternative samples generated with Powheg Box interfaced to Pythia v8.186 but with the radiation settings varied [99]. Finally an additional uncertainty associated with the choice of event generator is estimated by comparing the nominal samples with samples generated with MadGraph5_aMC@NLO interfaced to Pythia v8.186 [100]. For single-top-quark production an uncertainty is assigned to the treatment of the interference between the Wt and $t\bar{t}$ samples. This is done by comparing the nominal sample generated using the diagram removal method with a sample generated using the diagram subtraction method [99].

Of the systematic uncertainties considered in the EWK 2ℓ+0-jets search, uncertainties in the data-driven estimate of FNP leptons and theoretical uncertainties on the diboson WZ/ZZ backgrounds are not applied in this study as these processes represent small contributions to the subtracted backgrounds . Additional systematics are applied in the unfolding to account for the uncertainty in the normalisation of the top and VZ backgrounds, however the VZ normalisation uncertainties are observed to be negligible. The luminosity uncertainty (1.7%) is applied to the subtracted backgrounds that are not estimated using data-driven techniques.

Tests were performed to estimate the bias introduced by using information from the nominal signal MC in the unfolding procedure. This includes a data-driven test, whereby MC simulated WW signal events are reweighted at generator level to improve the agreement between the detector-level signal and the background-subtracted-data. The nominal unfolding procedure is then applied to the reweighted detector-level signal distributions to check whether the reweighted particle-level distributions can be reproduced. The impact of theoretical uncertainties on the signal modelling is evaluated by using the detector-level signal distributions with the alternative Sherpa $qq \rightarrow WW$ signal sample introduced in Section 3.1 as input to the nominal unfolding procedure, with the result compared to the alternative

particle-level signal distribution. In all tests the expected particle-level distributions were accurately recovered so no additional uncertainties on the unfolded results are applied.

Finally, statistical uncertainties on the data are calculated using pseudo-experiments that vary the data distributions according to their Poisson uncertainties in each bin, which are then passed through the unfolding calculation. Statistical uncertainties associated with the simulated MC samples are evaluated using a similar technique.

4 Results

The measured fiducial cross-section for $WW \to e^{\pm}\nu\mu^{\mp}\nu$ production for the phase space defined in Table 2 is:

$$\sigma_{WW\to e^{\pm}\nu\mu^{\mp}\nu} = 19.2 \pm 0.3\ (\text{stat})\ \pm 2.5\ (\text{syst})\ \pm 0.4\ (\text{lumi})\ \text{fb} = 19.2 \pm 2.6\ (\text{total})\ \text{fb}.$$

Of the categories of systematic uncertainties discussed in Section 3.5, the largest contribution is the experimental jet uncertainty which provides a 12% uncertainty on the measured fiducial cross-section. The higher jet uncertainties relative to the previous ATLAS 13 TeV WW+0-jet measurement [15] can be attributed to the lower p_{T} threshold used to define the jet veto. The measured value is compatible with the nominal predictions of Powheg Box v2 +Pythia 8.186 and Sherpa 2.2.2 (both combined with Sherpa v2.2.2 +OpenLoops (LO+PS) for the gg-initiated states) of 17.8 fb and 17.1 fb respectively. The ratio of the measured cross-section to the nominal Powheg Box v2 +Pythia 8.186 prediction is 1.08. To compare this to the detector-level WW normalisation factor of 1.25 ± 0.11 in the EWK 2ℓ+0-jets search [22] the normalisation factor of 1.25 must be divided by 1.13 to account for the NLO cross-section calculation, which is included in this study but not in the EWK 2ℓ+0-jets search. This gives 1.11 which is close to the value observed in this note.

Particle-level differential cross section for the six variables targeted in this study are presented in Figure 2 for the angular variables and Figure 3 for the scale variables. In each case, the right hand plot shows the impact of the uncertainties, grouped into the categories discussed in Section 3.5, on the measurement.

The dilepton rapidity distribution has a maximum between 0 and 1, consistent with the central production of a massive diboson system. The $|\Delta\phi_{e\mu}|$ distribution peaks at 2. The shape of this distribution is influenced by the m_{T2} selection defining the fiducial region: high $|\Delta\phi_{e\mu}|$ values are associated with back-to-back leptons which typically give lower m_{T2} values than are considered in this study. Conversely, the highest m_{T2} values (which for WW production should occur around 90 GeV in the absence of detector effects) are often associated with collinear leptons (low $|\Delta\phi_{e\mu}|$) which are also excluded from the fiducial region. The $\cos\theta^*$ distribution peaks around 0.8, with higher values being suppressed by the rapidity acceptance of the fiducial phase space. The scale variables all show the expected characteristic fall toward high values. The leading lepton and dilepton p_{T} are also suppressed at lower values due to the fiducial phase space cuts.

The measurements are compared to the qq-initiated NLO QCD+PS predictions from Powheg Box v2 +Pythia 8.186 and Sherpa v2.2.2, each combined with Sherpa v2.2.2 +OpenLoops (LO+PS) for the gg-initiated states. For the angular variables, the region with $|\Delta\phi_{e\mu}| < 1.5$ is underestimated by both theory predictions, which is consistent with observations in the previous ATLAS 13 TeV WW+0-jet measurement [15]. The region $\cos\theta^* > 0.8$ is also underestimated by 10-30% by both predictions. This corresponds to a rapidity difference between the leptons of $|\Delta y| \geq 2.2$. For the dilepton rapidity distribution $|y_{e\mu}|$ the theory shows reasonable agreement with the measurement. The predictions for the scale variables show good agreement with the data, with the exception of low values of $p_{\mathrm{T}}^{\mathrm{lead}\,\ell}$ where both predictions

underestimate the cross-section by 20-25%. Global χ^2 calculations are carried out for all predictions and are displayed in Table 3. Uncertainties in the theory predictions are not considered. The largest χ^2/NDF is 24.1 / 6 corresponding to the comparison between the $q\bar{q} \to WW$ (SHERPA 2.2.2) $+gg \to WW$ (SHERPA 2.2.2+OL) prediction and the unfolded distribution for $p_{\mathrm{T}}^{\mathrm{lead}\,\ell}$.

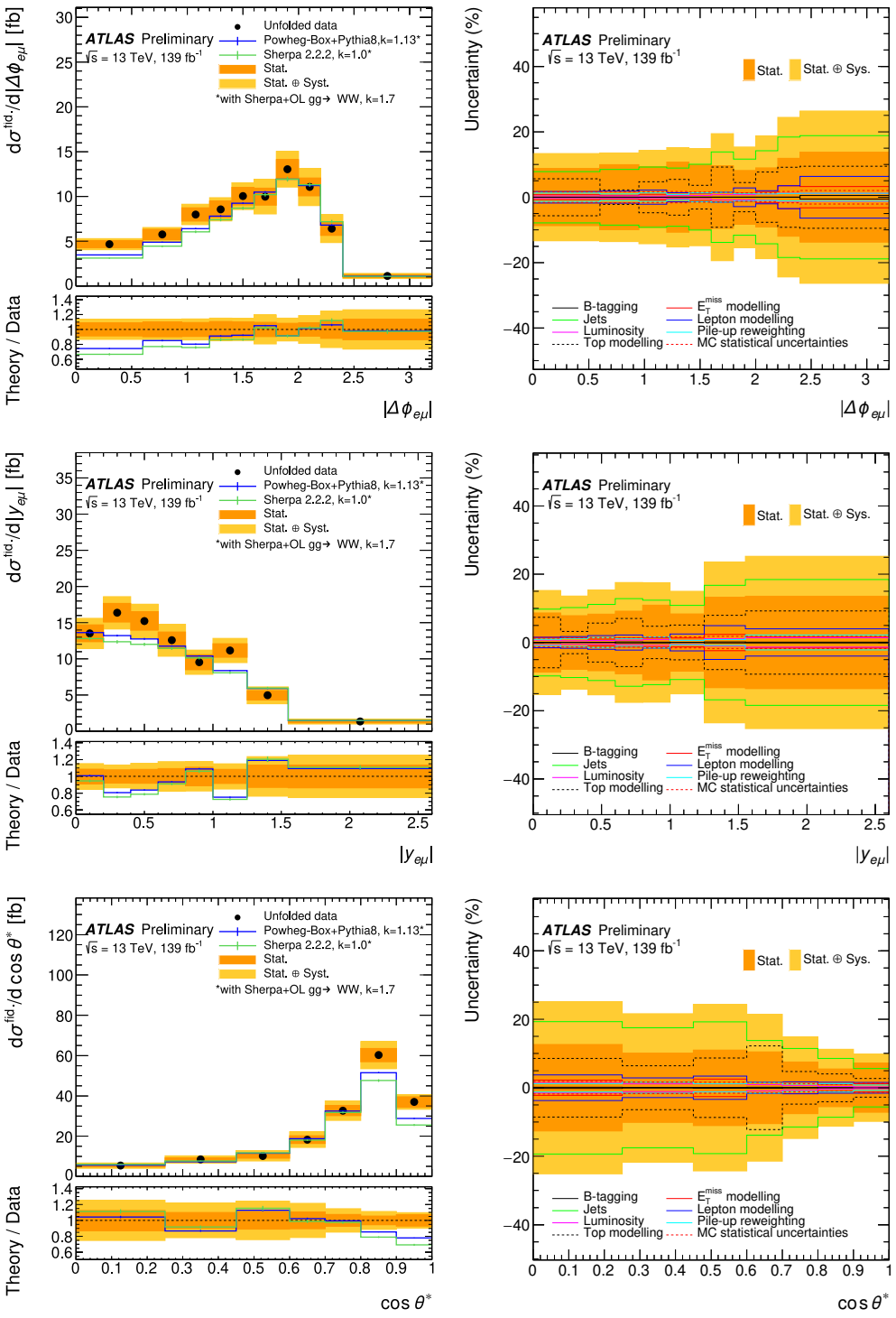

Figure 2: Measured fiducial differential cross-sections of WW production for (top to bottom) $|\Delta\phi(e\mu)|$, $|y_{e\mu}|$ and $\cos\theta^*$. The measured cross-section values are shown as points with error bars giving the statistical uncertainty and solid bands indicating the size of the total uncertainty. The results are compared to the $q\bar{q}$-initiated predictions from Powheg Box v2+ Pythia 8.186 and Sherpa v2.2.2, each combined with Sherpa v2.2.2 +OpenLoops (LO+PS) for the gg-initiated states. The k-factors refer to the corrections applied to scale the predictions of qq-initiated and gg-initiated processes to NNLO and NLO accuracy in QCD respectively. The right column shows a breakdown of contributions to the uncertainties on the unfolded measurement.

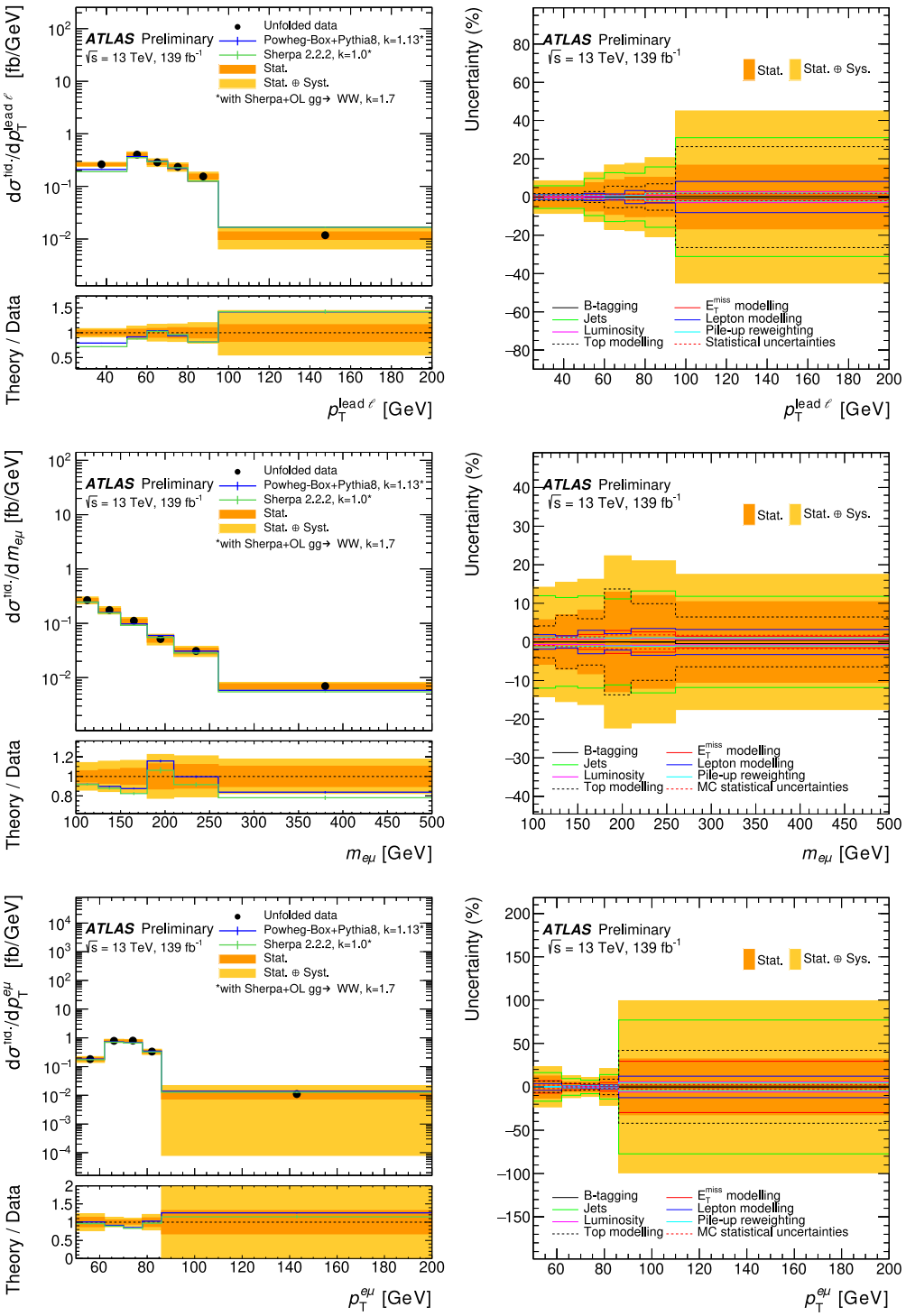

Figure 3: Measured fiducial differential cross-sections of WW production for (top to bottom) $p_{\mathrm{T}}^{\mathrm{lead}\,\ell}$, $m_{e\mu}$ and $p_{\mathrm{T}}^{e\mu}$. The last bin is inclusive in the measured observable and for $p_{\mathrm{T}}^{e\mu}$ the first bin contains the underflow bin. The measured cross-section values are shown as points with error bars giving the statistical uncertainty and solid bands indicating the size of the total uncertainty. The results are compared to the $q\bar{q}$-initiated predictions from Powheg Box v2+ Pythia 8.186 and Sherpa v2.2.2, each combined with Sherpa v2.2.2 +OpenLoops (LO+PS) for the gg-initiated states. The k-factors refer to the corrections applied to scale the predictions of qq-initiated and gg-initiated processes to NNLO and NLO accuracy in QCD respectively. The right column shows a breakdown of contributions to the uncertainties on the unfolded measurement.

Table 3: χ^2/NDF (number of degrees of freedom) for a comparison of unfolded distributions with different theory predictions. The calculation takes into account bin-by-bin correlations of systematic and statistical uncertainties. Uncertainties in the theory predictions are not considered.

	$\lvert\Delta\phi_{e\mu}\rvert$	$\lvert y_{e\mu}\rvert$	$\lvert\cos(\theta^*)\rvert$	$p_{\mathrm{T}}^{\mathrm{lead}\,\ell}$	$m_{e\mu}$	$p_{\mathrm{T}}^{e\mu}$
Powheg-Box+Pythia8 ($q\bar{q}$) & Sherpa 2.2.2 +OL (gg)	10.1 / 10	14.4 / 8	13.3 / 7	15.4 / 6	2.8 / 6	3.9 / 5
Sherpa 2.2.2 ($q\bar{q}$) & Sherpa 2.2.2 +OL (gg)	17.9 / 10	18.3 / 8	24.5 / 7	24.1 / 6	2.5 / 6	4.1 / 5

5 Conclusion

The cross-section for $WW \to e^{\pm}\nu\mu^{\mp}\nu$ production in pp collisions at $\sqrt{s} = 13$ TeV is measured in a fiducial phase space region characterised by the absence of jets and additional leptons, the presence of a high dilepton invariant mass $m_{e\mu}$, and with values of $E_{\mathrm{T}}^{\mathrm{miss}}$ and the stransverse mass m_{T2} motivated by the control regions of supersymmetry searches [22]. The measurement uses data collected by the ATLAS experiment at the LHC in 2015-2018, corresponding to an integrated luminosity of 139 fb^{-1}. The measured cross-section is $\sigma_{WW\to e^{\pm}\nu\mu^{\mp}\nu} = 19.2 \pm 0.3$ (stat) ± 2.5 (syst) ± 0.4 (lumi) fb. Differential cross-sections for three variables sensitive to the energy scale of the event and three variables sensitive to the angular correlations in the leptonic decay products are compared to two theoretical predictions from perturbative QCD calculations. No significant disagreements are observed in any of the distributions. This study has validated the SM in a new and interesting region motivated particularly by searches for supersymmetry and provided benchmark measurements that can be used to improve future SM predictions and calculate additional constraints on BSM models.

References

[1] Y. Golfand and E. Likhtman,
Extension of the Algebra of Poincare Group Generators and Violation of P Invariance,
JETP Lett. **13** (1971) 323, [Pisma Zh. Eksp. Teor. Fiz. **13** (1971) 452].

[2] D. Volkov and V. Akulov, *Is the neutrino a goldstone particle?*, Phys. Lett. B **46** (1973) 109.

[3] J. Wess and B. Zumino, *Supergauge transformations in four dimensions*,
Nucl. Phys. B **70** (1974) 39.

[4] J. Wess and B. Zumino, *Supergauge invariant extension of quantum electrodynamics*,
Nucl. Phys. B **78** (1974) 1.

[5] S. Ferrara and B. Zumino, *Supergauge invariant Yang-Mills theories*, Nucl. Phys. B **79** (1974) 413.

[6] A. Salam and J. Strathdee, *Super-symmetry and non-Abelian gauges*, Phys. Lett. B **51** (1974) 353.

[7] ATLAS Collaboration, *The ATLAS Experiment at the CERN Large Hadron Collider*,
JINST **3** (2008) S08003.

[8] ATLAS Collaboration, *Searches for scalar leptoquarks and differential cross-section measurements in dilepton–dijet events in proton–proton collisions at a centre-of-mass energy of* $\sqrt{s} = 13$ *TeV with the ATLAS experiment*, Eur. Phys. J. C **79** (2019) 733,
arXiv: 1902.00377 [hep-ex].

[9] ATLAS Collaboration, *Measurement of* W^+W^- *production in* pp *collisions at* $\sqrt{s} = 7$ *TeV with the ATLAS detector and limits on anomalous* WWZ *and* $WW\gamma$ *couplings*,
Phys. Rev. D **87** (2013) 112001, arXiv: 1210.2979 [hep-ex],
Erratum: Phys. Rev. D **88** (2013) 079906.

[10] CMS Collaboration, *Measurement of the* W^+W^- *cross section in* pp *collisions at* $\sqrt{s} = 7$ *TeV and limits on anomalous* $WW\gamma$ *and* WWZ *couplings*, Eur. Phys. J. C **73** (2013) 2610,
arXiv: 1306.1126 [hep-ex].

[11] ATLAS Collaboration,
Measurement of total and differential W^+W^- *production cross sections in proton–proton collisions at* $\sqrt{s} = 8$ *TeV with the ATLAS detector and limits on anomalous triple-gauge-boson couplings*,
JHEP **09** (2016) 029, arXiv: 1603.01702 [hep-ex].

[12] CMS Collaboration, *Measurement of the* W^+W^- *cross section in* pp *collisions at* $\sqrt{s} = 8$ *TeV and limits on anomalous gauge couplings*, Eur. Phys. J. C **76** (2016) 401,
arXiv: 1507.03268 [hep-ex].

[13] ATLAS Collaboration, *Measurement of* W^+W^- *production in association with one jet in proton–proton collisions at* $\sqrt{s} = 8$ *TeV with the ATLAS detector*, Phys. Lett. B **763** (2016) 114,
arXiv: 1608.03086 [hep-ex].

[14] ATLAS Collaboration, *Measurement of the* W^+W^- *production cross section in* pp *collisions at a centre-of-mass energy of* $\sqrt{s} = 13$ *TeV with the ATLAS experiment*, Phys. Lett. B **773** (2017) 354,
arXiv: 1702.04519 [hep-ex].

[15] ATLAS Collaboration, *Measurement of fiducial and differential* W^+W^- *production cross-sections at* $\sqrt{s} = 13$ *TeV with the ATLAS detector*, Eur. Phys. J. C **79** (2019) 884,
arXiv: 1905.04242 [hep-ex].

[16] ATLAS Collaboration, *Measurements of $W^+W^-+ \geq 1$ jet production cross-sections in pp collisions at $\sqrt{s} = 13$ TeV with the ATLAS detector*, JHEP **06** (2021) 003, arXiv: 2103.10319 [hep-ex].

[17] CMS Collaboration, *W^+W^- boson pair production in proton–proton collisions at $\sqrt{s} = 13$ TeV*, Phys. Rev. D **102** (2020) 092001, arXiv: 2009.00119 [hep-ex].

[18] ALEPH, DELPHI, L3 and OPAL Collaborations and the LEP Electroweak Working Group, *Electroweak measurements in electron–positron collisions at W-boson-pair energies at LEP*, Phys. Rept. **532** (2013) 119, arXiv: 1302.3415 [hep-ex].

[19] CDF Collaboration, *Observation of W^+W^- Production in $p\bar{p}$ collisions at $\sqrt{s} = 1.8$ TeV*, Phys. Rev. Lett. **78** (1997) 4536.

[20] CDF Collaboration, *Measurement of the W^+W^- Production Cross Section and Search for Anomalous $WW\gamma$ and WWZ Couplings in $p\bar{p}$ Collisions at $\sqrt{s} = 1.96$ TeV*, Phys. Rev. Lett. **104** (2010) 201801, [Erratum: Phys. Rev. Lett. 105 (2010) 019905], arXiv: 0912.4500 [hep-ex].

[21] DØ Collaboration, *Measurement of the WW Production Cross Section with Dilepton Final States in $p\bar{p}$ Collisions at $\sqrt{s} = 1.96$ TeV and Limits on Anomalous Trilinear Gauge Couplings*, Phys. Rev. Lett. **103** (2009) 191801, arXiv: 0904.0673 [hep-ex].

[22] ATLAS Collaboration, *Search for electroweak production of charginos and sleptons decaying into final states with two leptons and missing transverse momentum in $\sqrt{s} = 13$ TeV pp collisions using the ATLAS detector*, Eur. Phys. J. C **80** (2020) 123, arXiv: 1908.08215 [hep-ex].

[23] A. J. Barr, *Measuring slepton spin at the LHC*, JHEP **02** (2006) 042, arXiv: hep-ph/0511115.

[24] ATLAS Collaboration, *The ATLAS Collaboration Software and Firmware*, ATL-SOFT-PUB-2021-001, 2021, URL: https://cds.cern.ch/record/2767187.

[25] ATLAS Collaboration, *ATLAS data quality operations and performance for 2015–2018 data-taking*, JINST **15** (2020) P04003, arXiv: 1911.04632 [physics.ins-det].

[26] ATLAS Collaboration, *Luminosity determination in pp collisions at $\sqrt{s} = 13$ TeV using the ATLAS detector at the LHC*, ATLAS-CONF-2019-021, 2019, URL: https://cds.cern.ch/record/2677054.

[27] G. Avoni et al., *The new LUCID-2 detector for luminosity measurement and monitoring in ATLAS*, JINST **13** (2018) P07017.

[28] ATLAS Collaboration, *Performance of electron and photon triggers in ATLAS during LHC Run 2*, Eur. Phys. J. C **80** (2020) 47, arXiv: 1909.00761 [hep-ex].

[29] ATLAS Collaboration, *Performance of the ATLAS muon triggers in Run 2*, JINST **15** (2020) P09015, arXiv: 2004.13447 [hep-ex].

[30] ATLAS Collaboration, *The ATLAS Simulation Infrastructure*, Eur. Phys. J. C **70** (2010) 823, arXiv: 1005.4568 [physics.ins-det].

[31] GEANT4 Collaboration, S. Agostinelli et al., *GEANT4 – a simulation toolkit*, Nucl. Instrum. Meth. A **506** (2003) 250.

[32] ATLAS Collaboration, *Electron and photon performance measurements with the ATLAS detector using the 2015–2017 LHC proton–proton collision data*, JINST **14** (2019) P12006, arXiv: 1908.00005 [hep-ex].

[33] ATLAS Collaboration, *Muon reconstruction performance of the ATLAS detector in proton–proton collision data at* $\sqrt{s} = 13$ *TeV*, Eur. Phys. J. C **76** (2016) 292, arXiv: 1603.05598 [hep-ex].

[34] ATLAS Collaboration, *ATLAS b-jet identification performance and efficiency measurement with* $t\bar{t}$ *events in* pp *collisions at* $\sqrt{s} = 13$ *TeV*, Eur. Phys. J. C **79** (2019) 970, arXiv: 1907.05120 [hep-ex].

[35] P. Nason, *A new method for combining NLO QCD with shower Monte Carlo algorithms*, JHEP **11** (2004) 040, arXiv: hep-ph/0409146.

[36] S. Frixione, P. Nason and C. Oleari, *Matching NLO QCD computations with parton shower simulations: the POWHEG method*, JHEP **11** (2007) 070, arXiv: 0709.2092 [hep-ph].

[37] S. Alioli, P. Nason, C. Oleari and E. Re, *A general framework for implementing NLO calculations in shower Monte Carlo programs: the POWHEG BOX*, JHEP **06** (2010) 043, arXiv: 1002.2581 [hep-ph].

[38] T. Sjöstrand, S. Mrenna and P. Skands, *A brief introduction to PYTHIA 8.1*, Comput. Phys. Commun. **178** (2008) 852, arXiv: 0710.3820 [hep-ph].

[39] ATLAS Collaboration, *Measurement of the* Z/γ^* *boson transverse momentum distribution in* pp *collisions at* $\sqrt{s} = 7$ *TeV with the ATLAS detector*, JHEP **09** (2014) 145, arXiv: 1406.3660 [hep-ex].

[40] H.-L. Lai et al., *New parton distributions for collider physics*, Phys. Rev. D **82** (2010) 074024, arXiv: 1007.2241 [hep-ph].

[41] J. Pumplin et al., *New Generation of Parton Distributions with Uncertainties from Global QCD Analysis*, JHEP **07** (2002) 012, arXiv: hep-ph/0201195.

[42] ATLAS Collaboration, *Multi-Boson Simulation for* 13 *TeV ATLAS Analyses*, ATL-PHYS-PUB-2017-005, 2017, URL: https://cds.cern.ch/record/2261933.

[43] T. Gehrmann et al., *W^+W^- Production at Hadron Colliders in Next to Next to Leading Order QCD*, Phys. Rev. Lett. **113** (2014) 212001, arXiv: 1408.5243 [hep-ph].

[44] F. Buccioni et al., *OpenLoops 2*, Eur. Phys. J. C **79** (2019) 866, arXiv: 1907.13071 [hep-ph].

[45] F. Cascioli, P. Maierhöfer and S. Pozzorini, *Scattering Amplitudes with Open Loops*, Phys. Rev. Lett. **108** (2012) 111601, arXiv: 1111.5206 [hep-ph].

[46] A. Denner, S. Dittmaier and L. Hofer, *Collier: A fortran-based complex one-loop library in extended regularizations*, Comput. Phys. Commun. **212** (2017) 220, arXiv: 1604.06792 [hep-ph].

[47] F. Caola, K. Melnikov, R. Röntsch and L. Tancredi, *QCD corrections to W^+W^- production through gluon fusion*, Phys. Lett. B **754** (2016) 275, arXiv: 1511.08617 [hep-ph].

[48] E. Bothmann et al., *Event generation with Sherpa 2.2*, SciPost Phys. **7** (2019) 034, arXiv: 1905.09127 [hep-ph].

[49] R. D. Ball et al., *Parton distributions for the LHC run II*, JHEP **04** (2015) 040, arXiv: 1410.8849 [hep-ph].

[50] ATLAS Collaboration, *Improvements in $t\bar{t}$ modelling using NLO+PS Monte Carlo generators for Run 2*, ATL-PHYS-PUB-2018-009, 2018, URL: https://cds.cern.ch/record/2630327.

[51] ATLAS Collaboration, *Simulation of top-quark production for the ATLAS experiment at $\sqrt{s}$ = 13 TeV*, ATL-PHYS-PUB-2016-004, 2016, URL: https://cds.cern.ch/record/2120417.

[52] ATLAS Collaboration, *ATLAS simulation of boson plus jets processes in Run 2*, ATL-PHYS-PUB-2017-006, 2017, URL: https://cds.cern.ch/record/2261937.

[53] S. Frixione, P. Nason and G. Ridolfi, *A Positive-weight next-to-leading-order Monte Carlo for heavy flavour hadroproduction*, JHEP **09** (2007) 126, arXiv: 0707.3088 [hep-ph].

[54] S. Alioli, P. Nason, C. Oleari and E. Re, *A general framework for implementing NLO calculations in shower Monte Carlo programs: the POWHEG BOX*, JHEP **06** (2010) 043, arXiv: 1002.2581 [hep-ph].

[55] J. M. Campbell, R. K. Ellis, P. Nason and E. Re, *Top-pair production and decay at NLO matched with parton showers*, JHEP **04** (2015) 114, arXiv: 1412.1828 [hep-ph].

[56] T. Sjöstrand et al., *An introduction to PYTHIA 8.2*, Comput. Phys. Commun. **191** (2015) 159, arXiv: 1410.3012 [hep-ph].

[57] M. Czakon and A. Mitov, *Top++: A program for the calculation of the top-pair cross-section at hadron colliders*, Comput. Phys. Commun. **185** (2014) 2930, arXiv: 1112.5675 [hep-ph].

[58] ATLAS Collaboration, *ATLAS Pythia 8 tunes to 7 TeV data*, ATL-PHYS-PUB-2014-021, 2014, URL: https://cds.cern.ch/record/1966419.

[59] R. D. Ball et al., *Parton distributions with LHC data*, Nucl. Phys. B **867** (2013) 244, arXiv: 1207.1303 [hep-ph].

[60] E. Re, *Single-top Wt-channel production matched with parton showers using the POWHEG method*, Eur. Phys. J. C **71** (2011) 1547, arXiv: 1009.2450 [hep-ph].

[61] M. Aliev et al., *HATHOR – HAdronic Top and Heavy quarks crOss section calculatoR*, Comput. Phys. Commun. **182** (2011) 1034, arXiv: 1007.1327 [hep-ph].

[62] P. Kant et al., *HatHor for single top-quark production: Updated predictions and uncertainty estimates for single top-quark production in hadronic collisions*, Comput. Phys. Commun. **191** (2015) 74, arXiv: 1406.4403 [hep-ph].

[63] T. Melia, P. Nason, R. Rontsch and G. Zanderighi, *W^+W^-, WZ and ZZ production in the POWHEG BOX*, JHEP **11** (2011) 078, arXiv: 1107.5051 [hep-ph].

[64] P. Nason and G. Zanderighi, *W^+W^-, WZ and ZZ production in the POWHEG-BOX-V2*, Eur. Phys. J. C **74** (2014) 2702, arXiv: 1311.1365 [hep-ph].

[65] J. Pumplin et al.,
New generation of parton distributions with uncertainties from global QCD analysis,
JHEP **07** (2002) 012, arXiv: hep-ph/0201195 [hep-ph].

[66] D. de Florian et al.,
Handbook of LHC Higgs Cross Sections: 4. Deciphering the Nature of the Higgs Sector, (2016),
arXiv: 1610.07922 [hep-ph].

[67] C. Anastasiou et al.,
High precision determination of the gluon fusion Higgs boson cross-section at the LHC,
JHEP **05** (2016) 058, arXiv: 1602.00695 [hep-ph].

[68] C. Anastasiou, C. Duhr, F. Dulat, F. Herzog and B. Mistlberger,
Higgs Boson Gluon-Fusion Production in QCD at Three Loops,
Phys. Rev. Lett. **114** (2015) 212001, arXiv: 1503.06056 [hep-ph].

[69] F. Dulat, A. Lazopoulos and B. Mistlberger, *iHixs 2 – Inclusive Higgs cross sections*,
Comput. Phys. Commun. **233** (2018) 243, arXiv: 1802.00827 [hep-ph].

[70] U. Aglietti, R. Bonciani, G. Degrassi and A. Vicini,
Two-loop light fermion contribution to Higgs production and decays, Phys. Lett. B **595** (2004) 432,
arXiv: hep-ph/0404071.

[71] S. Actis, G. Passarino, C. Sturm and S. Uccirati,
NLO electroweak corrections to Higgs boson production at hadron colliders,
Phys. Lett. B **670** (2008) 12, arXiv: 0809.1301 [hep-ph].

[72] M. Bonetti, K. Melnikov and L. Tancredi, *Higher order corrections to mixed QCD-EW contributions to Higgs boson production in gluon fusion*, Phys. Rev. D **97** (2018) 056017,
arXiv: 1801.10403 [hep-ph], Erratum: Phys. Rev. D **97** (2018) 099906.

[73] J. Butterworth et al., *PDF4LHC recommendations for LHC Run II*, J. Phys. G **43** (2016) 023001,
arXiv: 1510.03865 [hep-ph].

[74] T. Gleisberg et al., *Event generation with SHERPA 1.1*, JHEP **02** (2009) 007,
arXiv: 0811.4622 [hep-ph].

[75] J. Alwall et al., *The automated computation of tree-level and next-to-leading order differential cross sections, and their matching to parton shower simulations*, JHEP **07** (2014) 079,
arXiv: 1405.0301 [hep-ph].

[76] ATLAS Collaboration,
Modelling of the $t\bar{t}H$ and $t\bar{t}V(V = W, Z)$ processes for $\sqrt{s} = 13$ TeV ATLAS analyses,
ATL-PHYS-PUB-2016-005, 2016, URL: https://cds.cern.ch/record/2120826.

[77] ATLAS Collaboration, *Monte Carlo Generators for the Production of a W or Z/γ^* Boson in Association with Jets at ATLAS in Run 2*, ATL-PHYS-PUB-2016-003, 2016,
URL: https://cds.cern.ch/record/2120133.

[78] R. Gavin, Y. Li, F. Petriello and S. Quackenbush,
FEWZ 2.0: A code for hadronic Z production at next-to-next-to-leading order, (2010) 2388,
arXiv: 1011.3540 [hep-ph].

[79] ATLAS Collaboration,
Topological cell clustering in the ATLAS calorimeters and its performance in LHC Run 1,
Eur. Phys. J. C **77** (2017) 490, arXiv: 1603.02934 [hep-ex].

[80] ATLAS Collaboration, *Jet energy scale and resolution measured in proton–proton collisions at $\sqrt{s}$ = 13 TeV with the ATLAS detector*, Eur. Phys. J. C **81** (2020) 689, arXiv: 2007.02645 [hep-ex].

[81] M. Cacciari, G. P. Salam and G. Soyez, *The anti-k_t jet clustering algorithm*, JHEP **04** (2008) 063, arXiv: 0802.1189 [hep-ph].

[82] M. Cacciari, G. P. Salam and G. Soyez, *FastJet user manual*, Eur. Phys. J. C **72** (2012) 1896, arXiv: 1111.6097 [hep-ph].

[83] ATLAS Collaboration, *Jet energy scale measurements and their systematic uncertainties in proton–proton collisions at $\sqrt{s}$ = 13 TeV with the ATLAS detector*, Phys. Rev. D **96** (2017) 072002, arXiv: 1703.09665 [hep-ex].

[84] ATLAS Collaboration, *Tagging and suppression of pileup jets with the ATLAS detector*, ATLAS-CONF-2014-018, 2014, URL: https://cds.cern.ch/record/1700870.

[85] ATLAS Collaboration, *Forward Jet Vertex Tagging: A new technique for the identification and rejection of forward pileup jets*, ATL-PHYS-PUB-2015-034, 2015, URL: https://cds.cern.ch/record/2042098.

[86] ATLAS Collaboration, *Selection of jets produced in 13 TeV proton–proton collisions with the ATLAS detector*, ATLAS-CONF-2015-029, 2015, URL: https://cds.cern.ch/record/2037702.

[87] ATLAS Collaboration, *Performance of pile-up mitigation techniques for jets in pp collisions at $\sqrt{s}$ = 8 TeV using the ATLAS detector*, Eur. Phys. J. C **76** (2016) 581, arXiv: 1510.03823 [hep-ex].

[88] ATLAS Collaboration, *Performance of missing transverse momentum reconstruction with the ATLAS detector using proton–proton collisions at $\sqrt{s}$ = 13 TeV*, Eur. Phys. J. C **78** (2018) 903, arXiv: 1802.08168 [hep-ex].

[89] C. G. Lester and D. J. Summers, *Measuring masses of semi-invisibly decaying particles pair produced at hadron colliders*, Phys. Lett. B **463** (1999) 99, arXiv: hep-ph/9906349.

[90] A. Barr, C. G. Lester and P. Stephens, *A variable for measuring masses at hadron colliders when missing energy is expected; m_{T2}: the truth behind the glamour*, J. Phys. G **29** (2003) 2343, arXiv: hep-ph/0304226.

[91] ATLAS Collaboration, *Object-based missing transverse momentum significance in the ATLAS Detector*, ATLAS-CONF-2018-038, 2018, URL: https://cds.cern.ch/record/2630948.

[92] ATLAS Collaboration, *Measurement of the top quark-pair production cross section with ATLAS in pp collisions at $\sqrt{s}$ = 7 TeV*, Eur. Phys. J. C **71** (2011) 1577, arXiv: 1012.1792 [hep-ex].

[93] M. Baak et al., *HistFitter software framework for statistical data analysis*, Eur. Phys. J. C **75** (2015) 153, arXiv: 1410.1280 [hep-ex].

[94] G. D'Agostini, *A multidimensional unfolding method based on Bayes' theorem*, Nucl. Instr. Meth. A **362** (1995) 487.

[95] G. D'Agostini, *Improved iterative Bayesian unfolding*, (2010), arXiv: 1010.0632 [physics.data-an].

[96] T. Adye, 'Unfolding algorithms and tests using RooUnfold',
Proceedings, 2011 Workshop on Statistical Issues Related to Discovery Claims in Search Experiments and Unfolding (PHYSTAT 2011) (CERN, Geneva, Switzerland, 17th–20th Jan. 2011) 313, arXiv: 1105.1160 [physics.data-an].

[97] M. Bähr et al., *Herwig++ physics and manual*, Eur. Phys. J. C **58** (2008) 639, arXiv: 0803.0883 [hep-ph].

[98] J. Bellm et al., *Herwig 7.0/Herwig++ 3.0 release note*, Eur. Phys. J. C **76** (2016) 196, arXiv: 1512.01178 [hep-ph].

[99] ATLAS Collaboration, *Studies on top-quark Monte Carlo modelling for Top2016*, ATL-PHYS-PUB-2016-020, 2016, URL: https://cds.cern.ch/record/2216168.

[100] ATLAS Collaboration,
Studies on top-quark Monte Carlo modelling with Sherpa and MG5_aMC@NLO, ATL-PHYS-PUB-2017-007, 2017, URL: https://cds.cern.ch/record/2261938.